magnetochemistry

Article

Facile Fabrication of PANI/$Fe_{2.85}Ni_{0.15}O_4$ Nanocomposites and Their Application for the Effective Degradation of Rhodamine B Dye

Do Hung Manh [1], Tran Minh Thi [2,3,*], Nguyen Thi Ngoc Anh [1], Vu Hong Ky [1], Nguyen Manh Nghia [4] and Tran Dang Thanh [1,*]

[1] Institute of Materials Science, Vietnam Academy of Science and Technology, Hanoi 100000, Vietnam; manhdh@ims.vast.ac.vn (D.H.M.); anhntn@ims.vast.ac.vn (N.T.N.A.); kyvh@ims.vast.ac.vn (V.H.K.)
[2] Institute for Theoretical and Applied Research, Duy Tan University, Hanoi 100000, Vietnam
[3] Faculty of Nature Science, Duy Tan University, Da Nang 550000, Vietnam
[4] Faculty of Physics, Hanoi National University of Education, Hanoi 100000, Vietnam; nghianm@hnue.edu.vn
* Correspondence: tranminhthi5@duytan.edu.vn (T.M.T.); thanhxraylab@yahoo.com (T.D.T.)

Abstract: Nanocomposites of polyaniline (PANI)/$Fe_{2.85}Ni_{0.15}O_4$ (PFN) were successfully prepared using the co-precipitation method combined with an in-situ polymerization process. The FN and PFN nanocatalysts were characterized using various methods for the photocatalytic degradation of Rhodamine B (RhB). The XRD, Raman, TEM, and DTA-DTG analyses suggest that the FN nanoparticles (NPs) were effectively coated by PANI and that there were interactions between FN and PANI. Magnetic measurements indicated that PFN nanocomposites exhibited good superparamagnetic behavior and high saturation magnetization (39.5–57.6 emu/g), which are suitable for separating photocatalysts from solution for reuse. Adsorption-desorption analysis showed that the specific surface area of PFN was higher than that of FN. The UV-vis absorption spectra of FN and PFN nanocomposites exhibited strong absorption of visible light, attributed to the doping of Ni, which resulted in the reduction of the band-gap energy (E_g) of Fe_3O_4 to 2.4 eV. PFN nanocomposites with different mass ratios of PANI demonstrated superior photocatalytic activity compared to FN NPs. Furthermore, it was observed that PFN with a 10% mass ratio of PANI exhibited the highest RhB degradation efficiency, achieving a rate of approximately 98% after 300 min of irradiation. Finally, the possible photocatalytic degradation mechanisms of the PFN nanocomposites on RhB were discussed. PFN photocatalysts with good photocatalytic activity, inexpensive materials, and easy preparation could be potential candidates for wastewater purification applications.

Keywords: PANI/$Fe_{2.85}Ni_{0.15}O_4$; polyaniline; magnetism; adsorption; photocatalysis

check for updates

Citation: Manh, D.H.; Thi, T.M.; Anh, N.T.N.; Ky, V.H.; Nghia, N.M.; Thanh, T.D. Facile Fabrication of PANI/$Fe_{2.85}Ni_{0.15}O_4$ Nanocomposites and Their Application for the Effective Degradation of Rhodamine B Dye. *Magnetochemistry* **2023**, *9*, 195. https://doi.org/10.3390/magnetochemistry9080195

Academic Editors: Manpreet Kaur and Meenu Arora

Received: 27 June 2023
Revised: 14 July 2023
Accepted: 28 July 2023
Published: 29 July 2023

1. Introduction

Rhodamine B (RhB) is one of the most toxic dyes. It is well-known for its stability and is widely used in the textile, leather, paper printing, paint, colored glass, and plastic industries [1,2]. RhB is a carcinogenic and neurotoxic dye capable of causing respiratory tract infections, skin and eye irritation, and gastrointestinal tract infections in animals and humans [3,4]. The most common methods used for dye removal are photocatalysis, filtration, chemical degradation, adsorption, biodegradation, and advanced oxidation processes (AOP), in which photocatalysis is an effective oxidation process for degrading organic compounds in aqueous solutions that are exposed to solar or artificial radiation [2,5–7].

Some metal oxides, such as TiO_2, ZnO, or complex transition metal oxides based on $BaTiO_3$ and their composites, etc., with several advantages, including photocatalytic activity as well as magnetism, have been investigated [8–15]. However, these materials have a large intrinsic band gap, which requires UV irradiation for photocatalytic activity, giving rise to very low energy efficiency in utilizing solar light, which makes them not cost-effective for

producing on an industrial scale. Meanwhile, the fast electron-hole recombination, resulting in a low quantum yield, causes lower photocatalytic efficiency. In addition, significant challenges include the difficulty of eliminating and reusing catalysts from the solution at the end of the process.

Iron oxide (Fe_3O_4, γ-Fe_2O_3) nanomaterials can solve the problem of catalyst separation from the solution due to their magnetic properties. However, only Fe_3O_4 contains Fe^{2+} in its structure, which helps improve the creation rate of reactive radicals (OH*) for effective reduction. Generally, Fe_3O_4 nanomaterials are considered effective heterogeneous photocatalysts because of their magnetic properties, catalytic activity, low cost, biocompatibility, and environmental friendliness [16–20].

Recently, transition metals such as Mn, Zn, Al [21–23], Sn [24], Cu [25], and Ni [26,27] have been introduced into the Fe_3O_4 structure to increase carrier lifetime and extend the absorption range of the photocatalyst towards the visible region. Among the transition metals, Ni dopant has been considered the most appropriate choice because the ionic radii of Ni^{2+} (0.69) and Fe^{2+} (0.77) are very similar, allowing Fe^{2+} to be replaced by Ni^{2+} in the crystal structure of Fe_3O_4 [27].

Polyaniline (PANI) is a conductive polymer with high conductivity, simple preparation, and reasonable stability. PANI can be combined with a wide range of organic/inorganic materials to form new sorbents (PANI-based materials) with higher removal efficiency for dyes and heavy metal ions. PANI-based nanocomposites, with many advantages such as low cost, environmental friendliness, and renewability, have proven their capability in a wide range of applications (removal of various heavy metal ions and dyes) [28–33].

To the best of our knowledge, PANI-based nanocomposites, such as MnO_2/PANI nanocables and PANI@Au, have been used for the effective photocatalytic degradation of RhB dye [34,35]. However, these materials are non-magnetic and therefore cannot be recovered by an external magnetic field. Though Lu et al. reported on the synthesis, structure, and magnetic properties of Fe_3O_4@PANI nanocomposites [36] in detail, the photocatalytic degradation of RhB dyes was not considered in their study. In addition, S. Xuan et al. [37] synthesized core/shell Fe_3O_4@PANI@Au nanocomposites using an ultrasound-assisted in-situ surface polymerization method and demonstrated the effective reduction of RhB. However, there are no reports on the fabrication and catalytic activity of PANI/Ni-doped Fe_3O_4 nanocomposites.

In the present study, PANI/$Fe_{2.85}Ni_{0.15}O_4$ (PFN) nanocomposites with different PANI mass ratios have been synthesized through the co-precipitation method combined with an in-situ polymerization process and characterized by different characterization techniques. Coating metal oxides (namely $Fe_{2.85}Ni_{0.15}O_4$ NPs) with PANI not only protects them but also reduces the band-gap energy (E_g) of nanocomposites. Our main aim is to evaluate the photocatalytic ability of these nanocomposites for the degradation of RhB dye. Following the structural studies, we then examine the effects of the PANI coating layer on the magnetic properties. Finally, we will investigate and discuss the photocatalytic ability of these nanocomposites for the degradation of RhB.

2. Materials and Methods

2.1. Sample Preparation

$FeCl_3 \cdot 6H_2O$, $FeCl_2 \cdot 4H_2O$, $Ni(CH_3COO)_2 \cdot 4H_2O$, and NaOH were used for the synthesis of Fe_3O_4 and $Fe_{2.85}Ni_{0.15}O_4$ nanoparticles (NPs) using the coprecipitation method [38]. Firstly, the reagents were mixed and dissolved in deionized water at specific concentrations, and the mixture was stirred under a nitrogen atmosphere. Furthermore, the mixture was heated to 80 °C, and the aqueous solution of NaOH was quickly added until reaching a pH of 13. After 30 min of reaction time, a dark solution was obtained. The precipitates were subsequently cooled to room temperature and separated using magnets. Finally, the precipitates were washed with distilled water and dried in an oven at 80 °C overnight. The Fe_3O_4 and $Fe_{2.85}Ni_{0.15}O_4$ NPs were labeled as F and FN, respectively.

Pure PANI was prepared by the polymerization method as detailed in Refs. [39,40]. PFN nanocomposites were prepared through a simple in situ polymerization method of PANI by aniline on the surface of FN nanoparticles [39,40], with mass ratios of PANI at 5, 10, and 15%. The synthesis procedure for PFN nanocomposites is as follows (Figure 1):

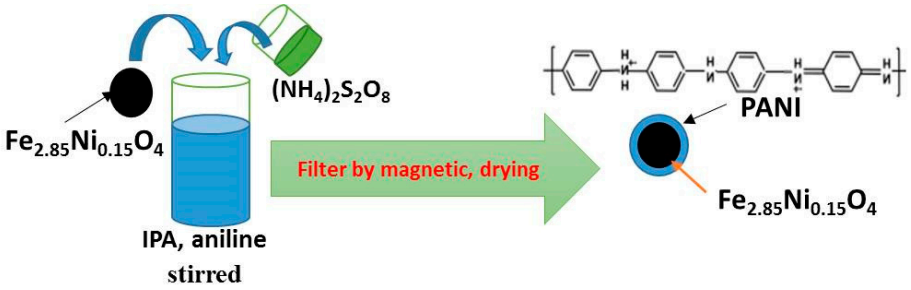

Figure 1. Flow chart for the synthesis of PANI/$Fe_{2.85}Ni_{0.15}O_4$ nanocomposites by in-situ polymerization method.

Step 1: 20 g of FN nanoparticles were added to 60 mL of distilled water, followed by the addition of 40 mL of isopropanol (IPA) and the appropriate mass of aniline. These mixtures were stirred well for 60 min to form solution A.

Step 2: A stoichiometric amount of $(NH_4)_2S_2O_8$ solution, with a monomer and oxidizing agent molar ratio of 1:1.5, was added dropwise to solution A. This resulted in a black-blue mixture (solution B) that was stirred for 2 h with an exothermic reaction.

Step 3: The solution was filtered using magnets, and the obtained solid was dried using a Labconco Freeze concentrator for 5 h at a pressure of 1 mPa and a temperature of −40 °C. The nanocomposites were labeled as PFN1, PFN2, and PFN3, corresponding to the PANI mass ratios of 5, 10, and 15%, respectively.

All precursors with high purity (≥98%) from Sigma Aldrich have been used to prepare samples.

2.2. Characterization

The typical XRD patterns of the samples were recorded using a Bruker D5500 with Cu-K_α radiation at a wavelength of λ = 0.154 Å. The morphology and particle size were characterized using a transmission electron microscope (TEM-JEOL5410). The chemical structure was identified using Raman spectra (LABRAM HR, laser Nd:YAG, λ = 785 nm with a power of 100 mW). The thermal stability was estimated using differential thermal analysis-thermogravimetry (DTA-TG) measurements (Shimadzu-DTG-60H). The magnetic properties were measured using a vibrating sample magnetometer (VSM). The specific surface areas were determined by the Brunauer-Emmett-Teller (BET) method through N_2 adsorption-desorption isotherms at 77 K using Micromeritics.

- Photocatalytic Testing

The photocatalytic activity of the as-prepared photocatalysts (FN, PFN1, PFN2, and PFN3) was tested by degrading RhB in an aqueous solution. In the photocatalytic experiment, 0.1 g of catalyst was dispersed in 100 mL of a RhB solution (10 ppm). Initially, the solution was magnetically stirred for 30 min to ensure a homogeneous mixture and was then placed in the dark to achieve adsorption-desorption equilibrium between the RhB dye and the catalyst. Subsequently, the solution was irradiated with visible light using a 300-W Xe lamp source with a wavelength range of 300–740 nm. The degradation of RhB was monitored at 30-minute intervals of irradiation time.

The experiments were carried out at room temperature under conditions of pH 7 in the solution mixture. The degradation of RhB was monitored by measuring the 555 nm absorbance peak intensities of the RhB solution using a UV-vis spectrophotometer (LABOMED UV-2602). The concentration of RhB in the solution was determined according to the Lambert-Beer law.

The relationship between reaction concentrations and time of the photocatalytic activities was calculated using the first-order kinetic model [41]:

$$\ln\left(\frac{C_0}{C}\right) = -k \quad (1)$$

where k is the first-order constant of the degradation process (k = slope), t is the radiation time, and C_0 and C are the RhB concentrations at initial and t times, respectively.

3. Results and Discussion

3.1. X-ray Diffraction Analysis

The room temperature XRD patterns of the F and FN nanoparticles (Figure 2a,b) reveal that both F (a) and FN (b) exhibit characteristic diffraction peaks at similar positions, which can be indexed to the (220), (311), (400), (422), (511), and (440) planes of an inverse spinel structure [42]. This indicates that the introduction of Ni^{2+} ions into the octahedral sites did not alter the characteristic spinel structure of Fe_3O_4 [43].

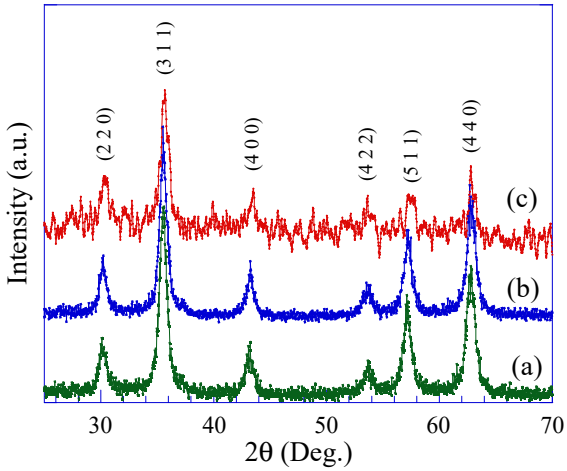

Figure 2. XRD patterns of samples: (a) Fe_3O_4, (b) FN, and (c) PFN2 nanocomposites.

The experimental lattice constant (a) was determined from the XRD data using Equation:

$$a = d_{hkl}\left(\sqrt{h^2 + k^2 + l^2}\right) \quad (2)$$

where (h, k, and l) are the Miller indices and d_{hkl} is the interplanar spacing. Applying Equation (2) to the peaks of (220), (311), (400), (422), (511), and (440), we get the average values of the lattice parameter a for F and FN of 8378 Å and 8371 Å, respectively. The decrease in lattice constant of FN compared to F can be attributed to the reduction in unit dimensions resulting from the partial substitution of Ni^{2+} ions (ionic radius of 0.69 Å) for Fe^{2+} ions (ionic radius of 0.77 Å) in Fe_3O_4 NPs [43].

The average crystalline size (D_{XRD}) was calculated using the Debye-Scherrer method for the most intense peak (311), according to Equation (3):

$$D_{XRD} = \frac{0.89\lambda}{\beta cos\theta} \quad (3)$$

where λ is the X-ray wavelength, β is the full width at half maximum (FWHM) of the peak, and θ is the Bragg angle. The calculated values for the D_{XRD} are 11.0 nm and 10.0 nm for F and FN, respectively.

In Figure 2c, the XRD pattern of the typical nanocomposite PFN2 (c) shows a background disturbance that corresponds to the presence of amorphous material (PANI). It is evident from the XRD pattern that the diffraction peak positions of FN nanoparticles remain

constant as they disperse in the PANI matrix during the in-situ polymerization reaction. The full width at half maximum of the XRD peaks is almost unchanged in all the samples. It implies that the average crystalline size in these samples is similar. Based on this XRD analysis, a core-shell structure can be assumed for the PANI/FN nanocomposites [39,40].

3.2. Raman Analysis

Raman spectroscopy is a valuable technique for studying the molecular binding properties of inorganic-based materials and conductive polymers [44]. In Figure 3, the room-temperature Raman spectra of PANI and a typical PFN nanocomposite (PFN2) are shown. The Raman spectrum of PANI exhibits peaks with strong intensity at 1163.73, 1333.69, 1497.03, and 1586.32 cm^{-1}, which are similar to those reported in [45]. The peak at 1586.32 cm^{-1} corresponds to the valence oscillation frequency of υC=C (aromatic) in the theoretical oxidation state, while the peak at 1497.03 cm^{-1} corresponds to the valence oscillation frequency of the C=N group. Similarly, the peaks at 1333.89, 1163.73, and 570.26 cm^{-1} are attributed to characteristic vibration groups of the υC-N^+, δC-H, and δC-H (aromatic) groups, respectively [45].

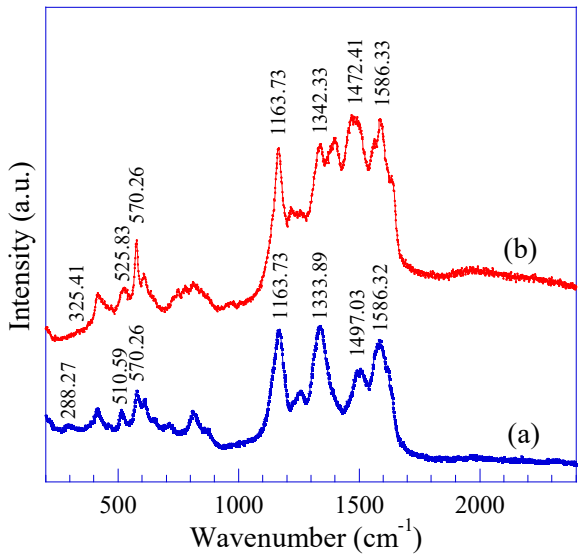

Figure 3. Raman spectra of (a) PANI and (b) PFN2 nanocomposites.

The Raman spectrum of the PFN2 nanocomposites is very similar to that of pure PANI. The peaks at 1586.33 and 1472.41 cm^{-1} fall within the wave number range of 1585–1630 cm^{-1} and 1480–1516 cm^{-1}, respectively, which are associated with the oscillation groups of υC=C (aromatic) and C=N in PANI. Similarly, the peaks at 1342.33, 1163.73, and 570.26 cm^{-1} correspond to the characteristic vibration groups of υC-N^+, δC-H, and δC-H (aromatic) in PANI, respectively. These Raman peaks are unsignificant in comparison with those of pure PANI. However, there are two small Raman peaks at 325.41 and 525.83 cm^{-1} on the Raman spectrum of the PFN2 nanocomposites, which are significantly shifted in comparison with those of pure PANI (288.27 and 510.59 cm^{-1}). These changes could be related to the E_g and T_{2g} modes of Fe-O bonds in magnetite [46], implying there were interactions between FN and PANI.

3.3. Morphology

The TEM images in Figure 4 reveal the uniform and spherical shape of FN NPs and a typical PFN nanocomposite (PFN2). No agglomeration is observed in the TEM images, indicating good dispersion of the nanoparticles. The particle sizes obtained from TEM data are consistent with the XRD results. The average particle size (D_{TEM}) of FN NPs is measured at 11 nm, while for the PFN2 nanocomposite, it is 20 nm. This suggests that

the FN NPs are coated with PANI through the in-situ polymerization process, forming a core-shell structure of the PFN nanocomposites [39,40].

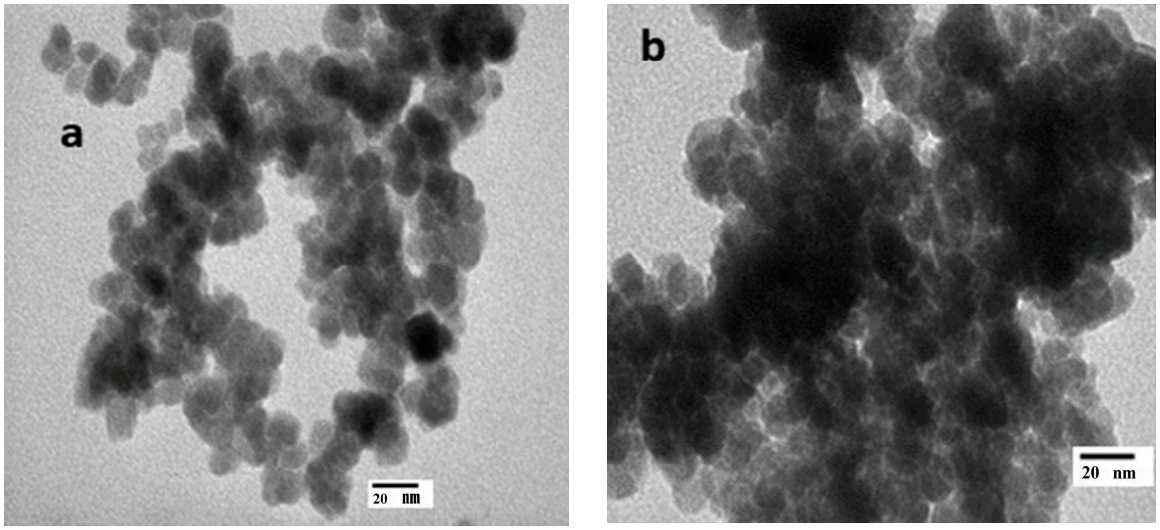

Figure 4. TEM images of (**a**) FN and (**b**) PFN2 nanocomposite.

3.4. DTA-DTG Analysis

The TGA-DTA curves of PANI and PFN2 nanocomposites are presented in Figure 5. In Figure 5a, the TGA curve of PANI exhibits a three-step weight loss. The first step occurs from T_{room} to 100 °C, in which the sharp endothermic peak occurs at 37.5 °C, corresponding to the evaporation of water. The second weight loss occurs from 100–352.4 °C (in the TGA curve); the sample mass decreased by about 31.7%, which may be related to the decomposition of PANI to form the monomers, oligomers, dimers, and trimers with the sharp endothermic peak at 290.6 °C in the DTG curve. The third weight loss occurs at 352.4–354.4 °C, and the mass of the sample continues to decrease by 9.8%. Moreover, strong thermal decomposition of the oligomer, dimers, and trimer happened, corresponding to the sharp endothermic peak at 554.2 °C in the DTG curve. These decompositions happen completely at temperatures above 600 °C.

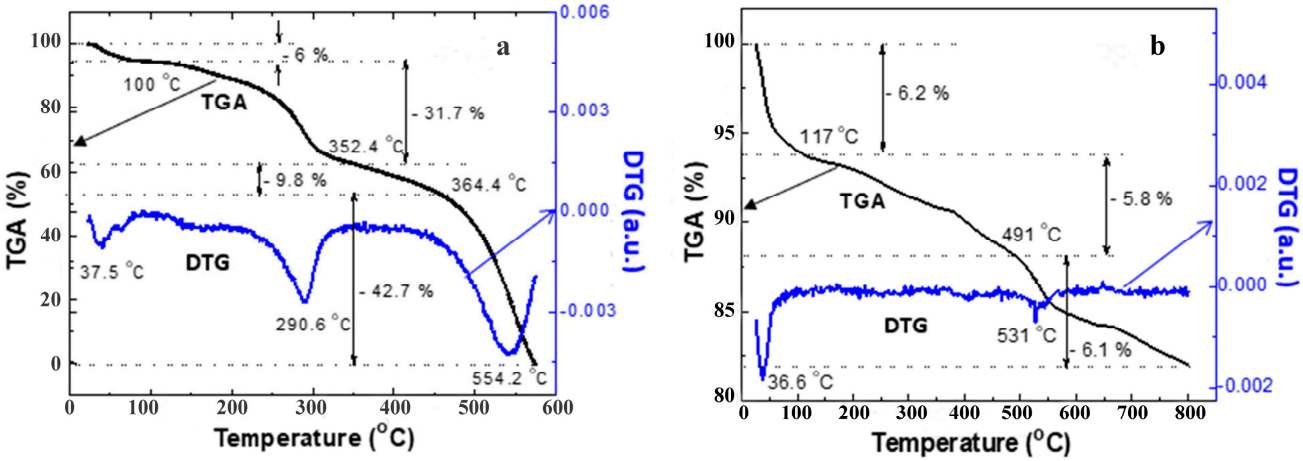

Figure 5. TGA/DTA curves of (**a**) PANI and (**b**) PFN2 nanocomposites.

The TGA-DTA curves of PFN2, as shown in Figure 5b, exhibit a two-stage weight loss behavior. The first stage occurs from room temperature to 100 °C, in which the 6.2% reduction in mass (TGA curve) resulted from water vapor evaporation in the sample, corresponding to a heat absorption peak at 36.6 °C (in the DTG curve). The second weight

loss stage occurs from 100–800 °C, with the 531 °C heat absorption peak on the DTG curve and significant decomposition of the composite structure [39]. In this stage, PANI decomposed completely above 600 °C, and the sample mass remained about 81.9% in the form of metal oxide.

Based on the analysis, it can be seen that the mass of the PFN2 sample decreased only 12% when the sample temperature increased to 491 °C, while the mass of the PANI sample decreased by 37.7% when the sample temperature increased to 352.4 °C. This indicates that the incorporation of ferrite nanoparticles with PANI greatly enhances the thermal stability of PFN2. The improved thermal stability can be attributed to the interaction between PANI and the ferrite nanoparticles, which restricts the thermal motion of PANI chains and hinders the crosslinking processes, thereby increasing the stability of the composite structure. This finding is consistent with the study conducted by Gabal et al. [40].

3.5. Magnetic Property Analysis

M(*H*) curves at room temperature for FN, FN1, FN2, and FN3 samples are shown in Figure 6. It shows that all these samples exhibit superparamagnetic behavior with a very low value of the remnant magnetization (M_r = 0.2–0.3 emu/g) and a quite high value of the saturation magnetization (M_S = 39.5–66.5 emu/g). The values of M_r and M_S obtained at room temperature for these samples are given in Table 1. Clearly, it is observed that FN nanoparticles exhibit good superparamagnetic behavior and a high value of M_S (66.5 emu/g at 10 kOe). The M_S value obtained for FN NPs in our work is smaller than that of $Ni_{0.11}Fe_{2.89}O_4$ NPs (M_S = 82.8 emu/g at 70 kOe) [43] but higher than that of $Ni_{0.20}Fe_{2.80}O_4$ NPs (M_S = 44.15 emu/g at 9 kOe) [47]. This difference may be due to the differences in Ni concentration and the applied magnetic field, although their crystalline sizes are quite similar. In addition, Yasemian et al. [47] also showed a monotonous decrease in saturation magnetization with particle size that increases with Ni concentration. However, the superparamagnetic behavior and the high M_S value obtained for our samples are suitable for the purpose of separating photocatalysts from solution. As the content of PANI in the nanocomposites increases, the saturation magnetization gradually decreases. This can be attributed to the decrease in the magnetic component percentage, accompanied by the increase in non-magnetic PANI layers on the surface of the FN NPs [39]. The presence of PANI in the nanocomposites introduces non-magnetic elements, leading to a reduction in the overall magnetic properties of the material.

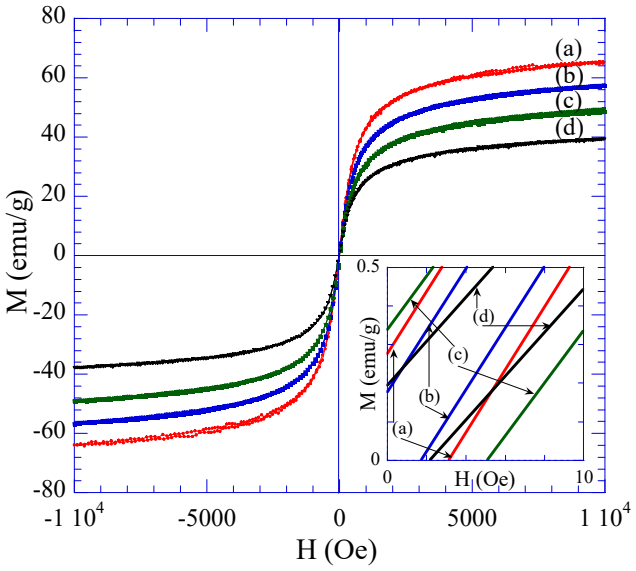

Figure 6. *M*(*H*) curves of samples: (**a**) FN, (**b**) PFN1, (**c**) PFN2, and (**d**) PFN3. The inset shows enlarged *M*(*H*) curves of samples.

Table 1. Specific surface area (SSA), saturation magnetization (M_S), remnant magnetization (M_r), band-gap energy (E_g), and first-order rate constant (k) of samples.

Sample Name	Mass Ratio of PANI in Nanocomposites (%)	SSA (m^2/g)	M_S (emu/g)	M_r (emu/g)	E_g (eV)	k ($\times 10^{-3}$ min^{-1})
FN	-	89.05	66.5	0.27	2.4	1.74
PFN1	5	98.25	57.6	0.18	2.1	2.27
PFN2	10	106.87	50.0	0.33	1.9	7.31
PFN3	15	98.88	39.5	0.19	1.8	6.17

3.6. Specific Surface Area Analysis

The surface area of the adsorbent plays a unique role in the adsorption study. The Brunauer-Emmett-Teller (BET) technique was employed to determine the average pore size and specific surface area of PANI, FN, and PFN nanocomposites via nitrogen adsorption-desorption analysis. The adsorption and desorption curves of PANI and a typical PFN nanocomposite (PFN2) are shown in Figure 7. The results obtained are summarized in Table 1.

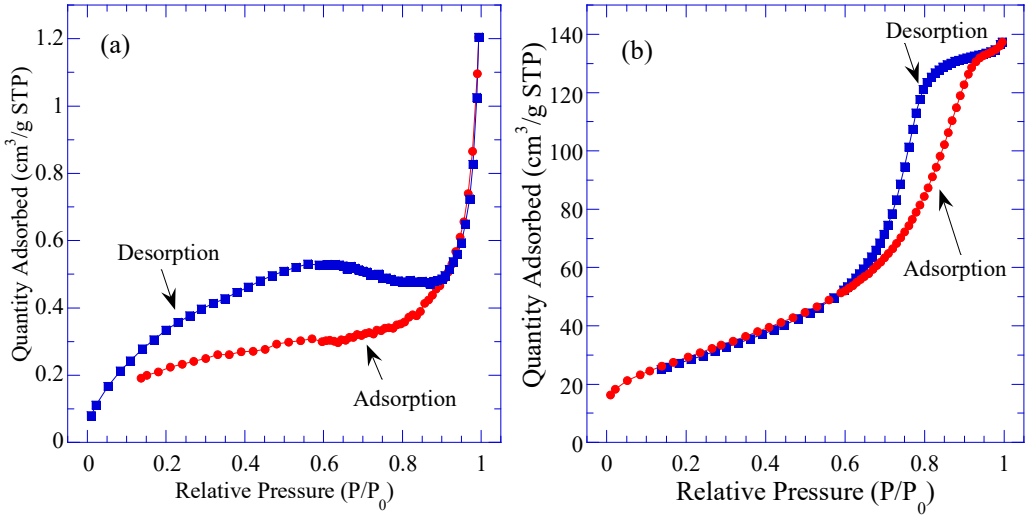

Figure 7. N2 adsorption-desorption isotherms of (**a**) PANI and (**b**) PFN2 nanocomposites.

The data shows that the specific surface area (SSA) of PFN2 nanocomposites is greater than that of PANI and FN NPs. PANI has a low SSA of 1.42 m^2/g, indicating it is a material with low porosity [45]. In contrast, the PFN nanocomposites have the corresponding high SSA values of 98.25, 106.87, and 98.88 m^2/g for PF1, PF2, and PF3, respectively, for highly porous materials. The relationship between the SSA of PFN nanocomposites and their photocatalytic activity will be discussed in the subsequent section.

3.7. UV-Vis Analysis

The UV-vis spectra of FN, PFN1, PFN2, and PFN3 provide information about the wavelength region in which the nanocatalyst absorbs light (Figure 8a). Koli et al. [41] reported that the Fe_3O_4 NPs exhibit absorption only in the ultraviolet (UV) region and weakly in the visible region due to their wide band-gap energy (E_g) of 3.0 eV. In this experiment, all the samples showed strong absorption in the visible region. The introduction of Ni doping in Fe_3O_4 leads to a reduction in the E_g value of Fe_3O_4, allowing for stronger absorption in the visible region and enhancing the photocatalytic process [41]. The reduced E_g value indicates that the nanocomposites are more efficient at utilizing visible light for photocatalytic reactions.

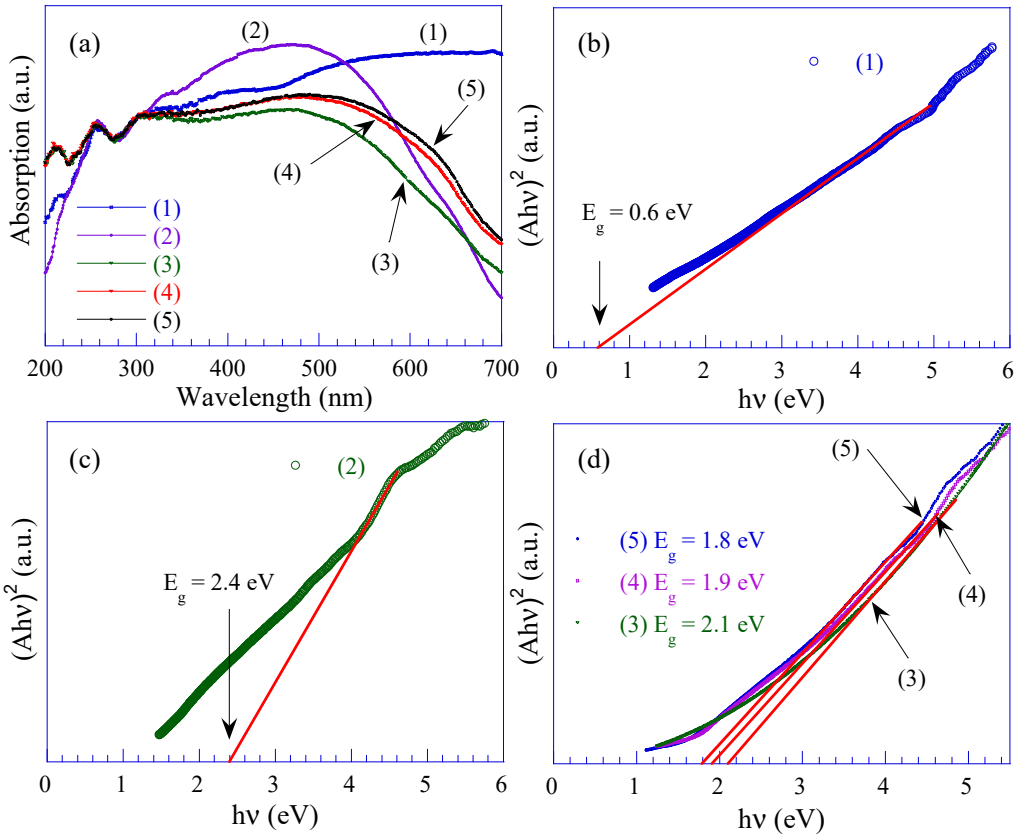

Figure 8. (**a**) UV-vis spectra and (**b**–**d**) Tauc plots for samples: (1) PANI, (2) FN, (3) PFN1, (4) PFN2, and (5) PFN3.

The Tauc equation was employed to quantitatively estimate the band gap [48]:

$$\alpha h\nu = A\left(h\nu - E_g\right)^2 \quad (4)$$

where α is the absorption coefficient, $h\nu$ is the photon energy, and A is a constant that does not depend on the photon energy. The Tauc plots in Figure 8b,c indicate that the E_g value decreases as the PANI mass ratio in the nanocomposites increases, namely 2.4, 2.1, 1.9, 1.8, and 0.6 eV for FN, PFN1, PFN2, PFN3, and PANI, respectively (Table 1). The decrease in E_g with increasing PANI content indicates the successful incorporation of PANI into the nanocomposites, which enhances their ability to absorb visible light and potentially improves their photocatalytic activity [48].

3.8. Photocatalytic Activity of PANI/FN Nanocomposites

During the first 30 min in the dark, a small amount of RhB (about a few percent) was adsorbed by the PFN nanocomposites. Furthermore, an adsorption-desorption equilibrium is established, and after that, the decrease in RhB concentration is due to the photocatalytic ability of the PFN nanocomposites when irradiated by an Xe lamp source. The photocatalytic degradation of RhB decreased as the time of visible light illumination increased (Figure 9a). In addition, the degradation rate of RhB in PFN nanocomposites increased with increasing PANI mass ratio to 10% and decreased with further increases in PANI mass ratio. Other reports [48,49] also showed that the loading amount of PANI relative to Sn_3O_4 had a significant impact on the photocatalytic activity efficiency. The degradation of RhB in 180 min is 75, 70, 40, and 29% for PFN2, PFN3, PFN1, and FN, respectively. This result showed that the best photocatalytic degradation efficiency of PFN2 was nearly 2.6 times higher than that of FN.

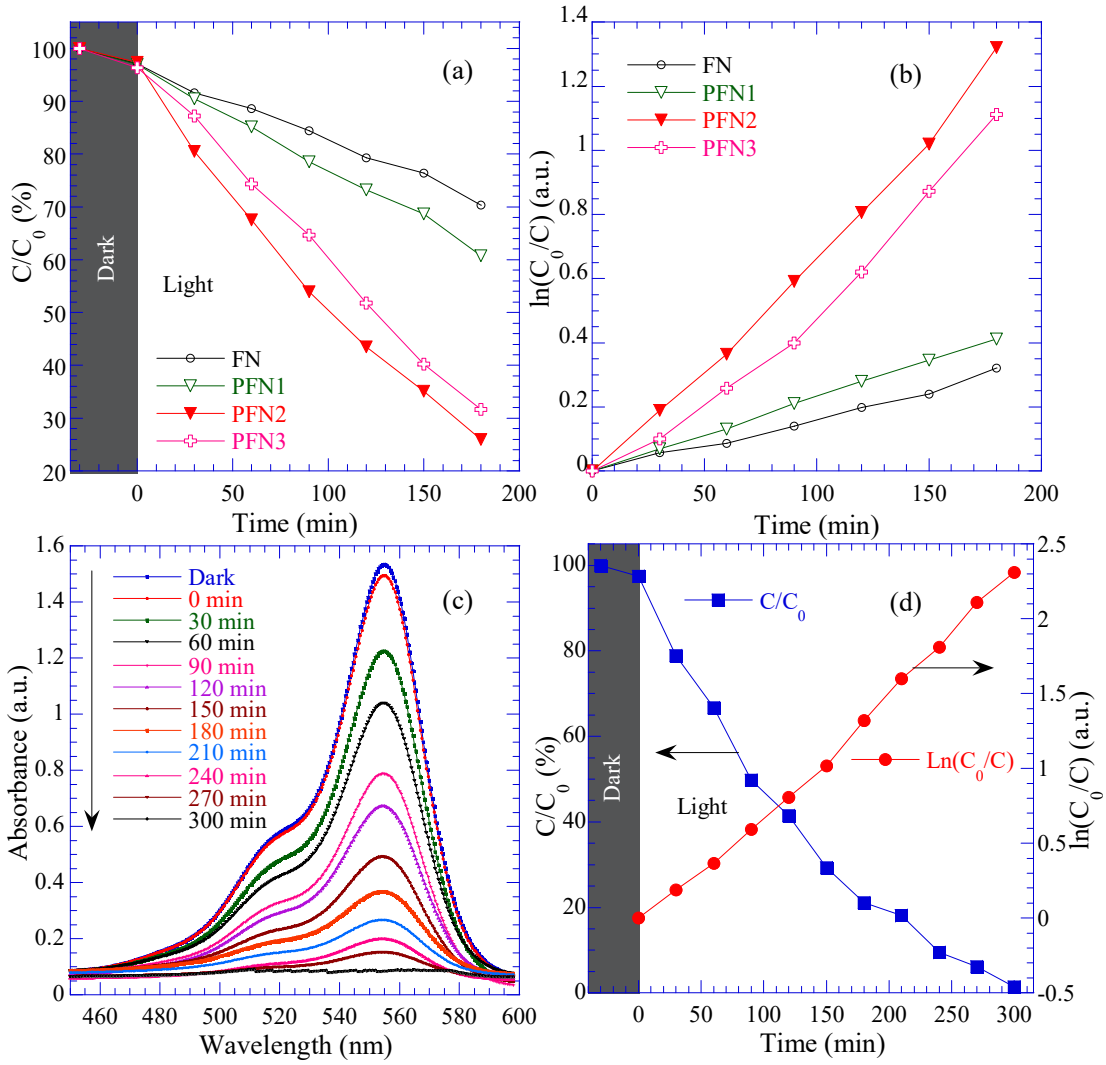

Figure 9. (**a**) Photocatalytic degradation under different photocatalysts. (**b**) The irradiation time (to 180 min) dependence of $\ln(C_0/C)$. (**c**) Temporal evolution of the RhB absorption spectra of PFN2; (**d**) Irradiation time (to 300 min) dependence of C/C_0 and $\ln(C_0/C)$ for PFN2.

The dependence of $\ln(C_0/C)$ over time for the catalysts is presented in Figure 9b. Assuming that the kinetic behavior of photocatalytic degradation follows a first-order kinetic rate equation (1), the rate constants (k) are calculated as 7.31, 6.17, 3.18, 2.27, and 1.74×10^{-3} min^{-1} for PFN2, PFN3, PFN1, and FN, respectively (Table 1). The first-order kinetic model fits the experimental data well. The degradation rate of RhB has a close correlation with the SSA and the photocatalytic efficiency. The PFN2 nanocomposite with the highest SSA value of 106.87 m^2/g exhibits the highest rate and photocatalytic activity in degrading RhB. Manfei et al. [48] suggested that the enlarged SSA of the PANI/Sn_3O_4 nanocomposites promotes the absorption of additional dye molecules, which is favorable to the dye degradation process.

The PFN2 nanocomposite with the highest photocatalytic ability was selected to investigate the photodegradation of the RhB for a longer time. After 300 min, the absorption spectrum of RhB showed that the decomposition had occurred almost completely (Figure 9c). The dependence of C/C_0 and $\ln(C_0/C)$ vs. time exhibited that the RhB decomposition rate is approximately 98% in 300 min of irradiation (Figure 9d).

In recent times, there have been several studies on the photocatalysis of nanocomposite materials for the degradation of RhB [50], Acid Blue 113 [51], Methylene Blue [52], and Bromophenol Blue [20]. The photocatalytic efficiency depends on different factors, such

as the dosage of adsorbents/photocatalysts, initial dye concentration, light source type, illumination power, and time. Therefore, it is challenging to compare photocatalytic results using different experimental conditions. For example, Matos et al. [53] reported that the photocatalytic efficiency reached 98% in 60 min using GF@CuS−Fe_3O_4 and H_2O_2. The research results in [54] indicated that the best photocatalytic efficiency (70%) using the TiO_2-$CoFe_2O_4$-PANI 3-component composite requires an illumination time of 7 h. Fatimah et al. [20] pointed out that the degradation efficiency of Bromophenol blue using Fe_3O_4-Fe_2O_3 nanocomposites and H_2O_2 approximated about 98% under both UV and visible light exposure in 60 min. Overall, the improved photocatalytic efficiency of polymer-inorganic nanocomposite could mainly be caused by the synergistic effects of PANI and inorganic. Our results show that PANI/$Fe_{2.85}Ni_{0.15}O_4$ is still competitive among the other photocatalysts to degrade organic dyes to some extent.

3.9. Photodegradation Mechanism

The mechanism of RhB photodegradation has been suggested in previous reports [48,55] and can be illustrated schematically in Figure 10. Briefly, when PFN photocatalysts are irradiated with a photon energy greater than the energy band gap, electrons in the valence band (VB) of FN nanoparticles and PANI can be excited to the conduction band (CB), resulting in the generation of e^- and h^+ in their VB and CB independently.

$$2PFN + h\nu \rightarrow PFN(e^-) + PFN(h^+)$$

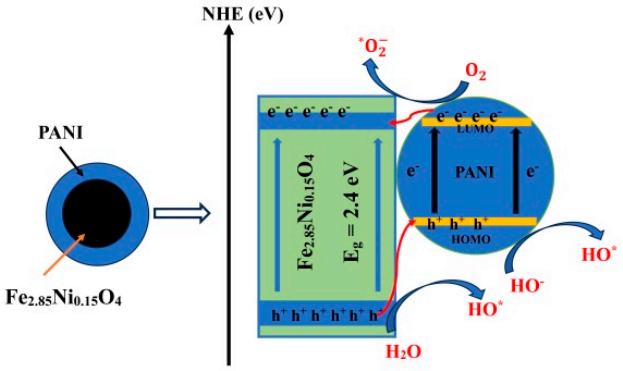

Figure 10. Schematic representation of the photocatalytic mechanism.

The hole in the VB diffuses to the surface, where it undergoes an oxidation reaction with RhB. Additionally, it reacts with water to produce an *OH-hydroxyl radical.

$$RhB + PFN(h^+) \rightarrow RhB+ + PFN$$

$$H_2O + PFN(h^+) \rightarrow *OH + H^+ + PFN$$

Electrons in the CB diffuse to the surface and undergo a reduction reaction with O_2. These reactions have created a very strong oxidizing *OH hydroxyl radical that can decompose organic substances on the surface of the photocatalyst.

$$PFN(e^-) + O_2 \rightarrow O^{2-}* + PFN$$

$$PFN(e^-) + O^{2-}* + H+ \rightarrow HO_2* + PFN$$

$$HO^{2*} + H+ \rightarrow H_2O_2$$

$$H_2O_2 + e^- \rightarrow * OH + OH^-$$

$$RhB + *OH \rightarrow CO_2 + H_2O$$

In addition, Manfei et al. [48] suggested that the improved photocatalytic efficiency is due to the formation of a p-n junction at the FN and PANI interfaces, which facilitates the optical transfer generated and effectively inhibits the photogenerated electron-hole pairs.

4. Conclusions

In summary, novel PANI/$Fe_{2.85}Ni_{0.15}O_4$ (PFN) nanocomposites with different PANI mass ratios were successfully prepared by the co-precipitation method combined with an in-situ polymerization process. XRD and Raman measurements confirmed the interaction between PANI and FN nanoparticles. TEM images, in agreement with the XRD data, led to the assumption that the nanocomposites had a core-shell structure, with the FN nanoparticles (approximately 10 nm in size) coated by PANI. Thermal analysis indicates that PANI thermal stability is improved by the presence of FN nanoparticles in nanocomposites. The magnetic measurements confirmed the superparamagnetic behavior and high saturation magnetization of the PFN nanocomposites. As a result, these nanocomposites can be easily separated from the solution due to their magnetic properties. Moreover, the presence of PANI in PFN nanocomposites significantly improves their photocatalytic activity. Furthermore, the PFN2 photocatalysts have the best photocatalytic efficiency of 98% on RhB in 300 min of visible light illumination. Finally, PFN photocatalysts with good photocatalytic activity, inexpensive materials, and easy preparation could be potential candidates for wastewater purification applications.

Author Contributions: D.H.M., T.M.T. and T.D.T.: conceptualization, methodology, formal analysis, writing—original draft, writing—review and editing. V.H.K., N.T.N.A. and N.M.N.: investigation, formal analysis, and review and editing. T.D.T.: supervised the project. All authors have read and agreed to the published version of the manuscript.

Funding: This work was supported by the Excellence Research Team Development Program grant funded by Vietnam Academy of Science and Technology (VAST) under Project Code NCXS01.04/22-24.

Institutional Review Board Statement: Not applicable.

Informed Consent Statement: Not applicable.

Data Availability Statement: Not applicable.

Conflicts of Interest: The authors declare no conflict of interest.

References

1. Sudarshan, S.; Bharti, V.S.; Harikrishnan, S.; Shukla, S.P.; Bhuvaneswari, G.R. Eco-toxicological effect of a commercial dye Rhodamine B on freshwater microalgae. *Chlorella vulgaris. Arch. Microbiol.* **2022**, *204*, 658. [CrossRef] [PubMed]
2. Al-Gheethi, A.A.; Azhar, Q.M.; Kumar, P.S.; Yusuf, A.A.; Buriahi, A.K.; Mohamed, R.M.S.R.; Shaibani, M.M. Sustainable approaches for removing Rhodamine B dye using agricultural waste adsorbents: A review. *Chemosphere* **2022**, *287*, 132080. [CrossRef] [PubMed]
3. Hamdaoui, O. Intensification of the sorption of Rhodamine B from aqueous phase by loquat seeds using ultrasound. *Desalination* **2011**, *271*, 279–286. [CrossRef]
4. Bhat, S.A.; Rashid, N.; Rather, M.A.; Bhat, S.A.; Ingole, P.P.; Bhat, M.A. Highly efficient catalytic reductive degradation of Rhodamine-B over Palladium-reduced graphene oxide nanocomposite. *Chem. Phys. Lett.* **2020**, *754*, 137724. [CrossRef]
5. Maji, N.; Dosanjh, H.S. Ferrite Nanoparticles as Catalysts in Organic Reactions: A Mini Review. *Magnetochemistry* **2023**, *9*, 156. [CrossRef]
6. Shahabuddin, S.; Sarih, N.M.; Ismail, F.H.; Shahid, M.M.; Huang, N.M. Synthesis of chitosan grafted-polyaniline/Co_3O_4 nanocube nanocomposites and their photocatalytic activity toward methylene blue dye degradation. *RSC Adv.* **2015**, *5*, 83857–83867. [CrossRef]
7. Zhou, M.; Han, D.; Liu, X.; Ma, C.; Wang, H.; Tang, Y.; Huo, P.; Shi, W.; Yan, Y.; Yang, J. Enhanced visible light photocatalytic activity of alkaline earth metal ions-doped CdSe/RGO photocatalysts synthesized by hydrothermal method. *App. Catal.* **2015**, *172*, 174–184. [CrossRef]
8. Nam, Y.; Lim, J.H.; Ko, K.C.; Lee, J.Y. Photocatalytic activity of TiO_2 nanoparticles: A theoretical aspect. *J. Mater. Chem. A* **2019**, *7*, 13833–13859. [CrossRef]
9. Pawar, M.; Sendogdular, S.T.; Gouma, P.A. Brief Overview of TiO_2 Photocatalyst for Organic Dye Remediation: Case Study of Reaction Mechanisms Involved in Ce-TiO_2 Photocatalysts System. *J. Nanomater.* **2018**, *2018*, 5953609.

10. Khokhra, R.; Bharti, B.; Lee, H.N.; Kumar, R. Visible and UV photo-detection in ZnO nanostructured thin films via simple tuning of solution method. *Sci. Rep.* **2017**, *7*, 15032. [CrossRef]
11. Ong, C.B.; Ng, L.Y.; Mohammad, A.W. A review of ZnO nanoparticles as solar photocatalysts: Synthesis, mechanisms and applications. *Renew. Sustain. Energy Rev.* **2018**, *81*, 536–551. [CrossRef]
12. Danish, M.S.S.; Estrella, L.L.; Alemaida, I.M.A.; Moiseev, L.N.; Ahmadi, M.; Nazari, M.; Wali, M.; Zaheb, H.; Senjyu, T. Photocatalytic Applications of Metal Oxides for Sustainable Environmental Remediation. *Metals* **2021**, *11*, 80. [CrossRef]
13. Trukhanov, S.V.; Trukhanov, A.V.; Salem, M.M.; Trukhanova, E.L.; Panina, L.V.; Kostishyn, V.G.; Darwish, M.A.; Trukhanov, A.V.; Zubar, T.I.; Tishkevich, D.I.; et al. Preparation and investigation of structure, magnetic and dielectric properties of $(BaFe_{11.9}Al_{0.1}O_{19})_{1-x}$-$(BaTiO_3)_x$ bicomponent ceramics. *Ceram. Int.* **2018**, *44*, 21295–21302. [CrossRef]
14. Wang, P.J.; Zhou, D.; Li, J.; Pang, L.X.; Liu, W.F.; Su, J.Z.; Singh, C.; Trukhanov, S.; Trukhanov, A. Significantly enhanced electrostatic energy storage performance of P (VDF-HFP)/$BaTiO_3$-$Bi(Li_{0.5}Nb_{0.5})O_3$ nanocomposites. *Nano Energy* **2020**, *78*, 105247. [CrossRef]
15. Karpinsky, D.V.; Silibin, M.V.; Trukhanov, S.V.; Trukhanov, A.V.; Zhaludkevich, A.L.; Latushka, S.I.; Zhaludkevich, D.V.; Khomchenko, V.A.; Alikin, D.O.; Abramov, A.S.; et al. Peculiarities of the crystal structure evolution of $BiFeO_3$-$BaTiO_3$ ceramics across structural phase transitions. *Nanomaterials* **2020**, *10*, 801. [CrossRef] [PubMed]
16. Anbari, R.; Obaidy, A.; Abd, E. Photocatalytic activity of Fe_3O_4 under solar radiation. *Mesop. Environ. J.* **2016**, *2*, 41–53.
17. Liu, M.; Ye, Y.; Ye, J.; Gao, T.; Wang, D.; Chen, G.; Song, Z. Recent Advances of Magnetite (Fe_3O_4)-Based Magnetic Materials in Catalytic Applications. *Magnetochemistry* **2023**, *9*, 110. [CrossRef]
18. Rajput, S.; Pittman, C.U.; Mohan, D. Magnetic magnetite (Fe_3O_4) nanoparticle synthesis and applications for lead (Pb^{2+}) and chromium (Cr^{6+}) removal from water. *J. Colloid Interface Sci.* **2016**, *468*, 334–346. [CrossRef]
19. Kore, R.; Sawant, A.D.; Rogers, R.D. Recyclable magnetic Fe_3O_4 nanoparticle-supported chloroaluminate ionic liquids for heterogeneous lewis acid catalysis. *ACS Sustain. Chem. Eng.* **2021**, *9*, 8797–8802. [CrossRef]
20. Fatimah, I.; Pratiwi, E.Z.; Wicaksono, W.P. Synthesis of magnetic nanoparticles using Parkia speciosa Hassk pod extract and photocatalytic activity for Bromophenol blue degradation. *Egypt. J. Aquat. Res.* **2020**, *46*, 35–40. [CrossRef]
21. Abbas, M.; Torati, S.R.; Rao, B.P.; Abdel-Hamed, M.O.; Kim, C. Size Controlled Sonochemical Synthesis of Highly Crystalline Superparamagnetic Mn-Zn Ferrite Nanoparticles in Aqueous Medium. *J. Alloys Compd.* **2015**, *644*, 774–782. [CrossRef]
22. Cynthia, W.C.; Warner, L.; Mackie, E.K.; Neiner, D.; Saraf, V.L.; Addleman, S.R. Manganese Doping of Magnetic Iron Oxide Nanoparticles: Tailoring Surface Reactivity for a Regenerable Heavy Metal Sorbent. *Langmuir* **2012**, *28*, 3931–3937.
23. Borhan, A.I.; Samoila, P.; Hulea, V.; Iordan, A.R.; Palamaru, M.N. Correlation between Structural, Magnetic and Electrical Properties of Nanocrystalline Al^{3+} Substituted Zinc Ferrite. *J. Taiwan Inst. Chem.* **2014**, *45*, 1655–1660. [CrossRef]
24. Cao, Z.; Qin, M.; Gu, Y.; Jia, B.; Chen, P.; Qu, X. Synthesis and characterization of Sn-doped hematite as visible light photocatalyst. *Mater. Res. Bull.* **2016**, *77*, 41–47. [CrossRef]
25. Rahmayeni; Wendari, T.P.; Atmoko, H.M.; Stiadi, Y.; Putri, Y.E.; Zulhadjri. $CuFe_2O_4$/activated carbon nanocomposite for efficient photocatalytic degradation of dye: Green synthesis approaches using the waste of oil palm empty bunches and bio-capping agent. *Case Stud. Chem. Environ. Eng.* **2023**, *7*, 100305. [CrossRef]
26. Oktavia, S.H.; Cahyana, A.H.; Hapsari, M.; Yunarti, R.T.; Liandi, A.R. Synthesis and antimicrobial activity of spiro-oxindole-chromene derivative compounds based curcuminoid and chalcone. *Rasayan J. Chem.* **2021**, *14*, 1990–1997. [CrossRef]
27. Lassoued, A.; Lassoued, M.S.; Granda, S.G.; Dkhil, B.; Ammar, S.; Gadri, A. Synthesis and characterization of Ni-doped α-Fe_2O_3 nanoparticles through co-precipitation method with enhanced photocatalytic activities. *J. Mater. Sci. Mater. Electron.* **2016**, *29*, 5726–5737. [CrossRef]
28. Eskandari, E.; Kosari, M.; Farahani, M.H.D.A.; Khiavi, N.D.; Saeeidikhani, M.; Katal, R.; Zarinejad, M. A Review on Polyaniline-based Materials Applications in Heavy Metals Removal and Catalytic Processes. *Sep. Purif. Technol.* **2020**, *231*, 115901. [CrossRef]
29. Karthik, R.; Meenakshi, S. Biosorption of Pb (II) and Cd (II) ions from aqueous solution using polyaniline/chitin composite. *Sep. Sci. Technol.* **2016**, *51*, 733–742. [CrossRef]
30. Qiu, B.; Xu, C.; Sun, D.; Yi, H.; Guo, J.; Zhang, X.; Qu, H.; Guerrero, M.; Wang, X.; Noel, N. Polyaniline coated ethyl cellulose with improved hexavalent chromium removal. *ACS Sustain. Chem. Eng.* **2014**, *2*, 2070–2080. [CrossRef]
31. Pandimurugan, R.; Thambidurai, S. Synthesis of seaweed-ZnO-PANI hybrid composite for adsorption of methylene blue dye. *J. Environ. Chem. Eng.* **2016**, *4*, 1332–1347. [CrossRef]
32. Afshar, A.; Sadjadi, S.A.S.; Mollahosseini, A.; Eskandarian, M.R. Polypyrrole-polyaniline/Fe_3O_4 magnetic nanocomposite for the removal of Pb (II) from aqueous solution. *Korean J. Chem. Eng.* **2016**, *33*, 669–677. [CrossRef]
33. Moosavian, M.A.; Moazezi, N. Removal of cadmium and zinc ions from industrial wastewater using nanocomposites of PANI/ZnO and PANI/CoHCF: A comparative study. *Desalin. Water Treat.* **2016**, *57*, 20817–20836.
34. Han, J.; Wang, M.; Cao, S.; Fang, P.; Lu, S.; Chen, R.; Guo, R.J.J.M.C.A. Reactive template strategy for fabrication of MnO_2/polyaniline coaxial nanocables and their catalytic application in the oxidative decolorization of rhodamine B. *J. Mater. Chem. A* **2013**, *1*, 13197–13202. [CrossRef]
35. Zhang, B.; Zhao, B.; Huang, S.; Zhang, R.; Xu, P.; Wang, H.L. One-pot interfacial synthesis of Au nanoparticles and Au–polyaniline nanocomposites for catalytic applications. *Cryst. Eng. Comm.* **2012**, *14*, 1542–1544. [CrossRef]
36. Lu, X.; Yu, Y.; Chen, L.; Mao, H.; Gao, H.; Wang, J.; Zhang, W.; Wei, Y. Aniline dimer–COOH assisted preparation of well-dispersed polyaniline–Fe_3O_4 nanoparticles. *Nanotechnology* **2005**, *16*, 1660. [CrossRef]

37. Xuan, S.; Wang, Y.X.J.; Yu, J.C.; Leung, K.C.F. Preparation, characterization, and catalytic activity of core/shell Fe_3O_4@ polyaniline@ Au nanocomposites. *Langmuir* **2009**, *25*, 11835–11843. [CrossRef]
38. Phong, L.T.H.; Manh, D.H.; Nam, P.H.; Lam, V.D.; Khuyen, B.X.; Tung, B.S.; Bach, T.N.; Tung, D.K.; Phuc, N.X.; Hung, T.V.; et al. The-Long Phan and Manh Huong Phan, Structural, magnetic and hyperthermia properties and their correlation in cobalt-doped magnetite nanoparticles. *RSC Adv.* **2022**, *12*, 698. [CrossRef]
39. Gabal, M.A.; Al-Juaid, A.A.; El-Rashed, S.; Hussein, M.A.; Al-Angari, Y.M. Polyaniline/$Co_{0.6}Zn_{0.4}Fe_2O_4$ core-shell nanocomposites, Synthesis, characterization and properties. *J. Alloys Compd.* **2018**, *747*, 83–90. [CrossRef]
40. Gabal, M.A.; Hussein, M.A.; Hermas, A.A. Synthesis, Characterization and Electrical Conductivity of Polyaniline-$Mn_{0.8}Zn_{0.2}Fe_2O_4$ Nano-composites. *Int. J. Electrochem. Sci.* **2016**, *11*, 4526–4538. [CrossRef]
41. Koli, P.B.; Kapadnis, K.H.; Deshpande, U.G. Transition metal decorated Ferrosoferric oxide (Fe_3O_4): An expeditious catalyst for photodegradation of Carbol Fuchsin in environmental remediation. *J. Environ. Chem. Eng.* **2019**, *7*, 103373. [CrossRef]
42. Phong, P.T.; Oanh, V.T.K.; Lam, T.D.; Phuc, N.X.; Tung, L.D.; Thanh, N.T.K.; Manh, D.H. Iron Oxide Nanoparticles: Tunable Size Synthesis and Analysis in Terms of the Core–Shell Structure and Mixed Coercive Model. *J. Elec. Mater.* **2017**, *46*, 2533. [CrossRef]
43. Larumbe, S.; Gómez-Polo, C.; Pérez-Landazábal, J.I.; García-Prieto, A.; Alonso, J.; Fdez-Gubieda, M.L.; Cordero, D.; Gómez, J. Ni Doped Fe_3O_4 Magnetic Nanoparticles. *J. Nanosci. Nanotechnol.* **2012**, *12*, 2652–2660. [CrossRef] [PubMed]
44. Rajagopalan, B.; Hur, S.H.; Chung, J.S. Surfactant-treated graphene covered polyaniline nanowires for supercapacitor electrode. *Nanoscale Res. Lett.* **2015**, *10*, 183. [CrossRef]
45. Brun, M.; Lallemand, A.; Quinson, J.-F.; Eyraud, C. A new method for the simultaneous determination of the size and the shape of pores: The Thermoporometry. *Thermochim. Acta* **1977**, *88*, 85122. [CrossRef]
46. Guo, C.; Hu, Y.; Qian, H.; Ning, J.; Xu, S. Magnetite (Fe_3O_4) tetrakaidecahedral microcrystals: Synthesis, characterization, and micro-Raman study. *Mater. Charact.* **2011**, *62*, 148–151. [CrossRef]
47. Yasemian, A.R.; Kashi, M.A.; Ramazani, A. Hyperthermia properties of $Ni_xFe_{3-x}O_4$ nanoparticles: A first-order reversal curve investigation. *J. Mater. Sci. Mater. Electron.* **2019**, *30*, 21278–21287. [CrossRef]
48. Manfei, L.; Yang, L.; Wang, X.; Cheng, X.; Song, Y.; Yin, Y.; Liu, H.; Han, Y.; Cao, K.; Ma, W.; et al. Visible-light photocatalytic capability and the mechanism investigation of a novel PANI/Sn_3O_4 p–n heterostructure. *RSC Adv.* **2019**, *9*, 40694.
49. Zhang, H.; Zhu, Y. Significant Visible Photoactivity and Antiphotocorrosion Performance of CdS Photocatalysts after Monolayer Polyaniline Hybridization. *J. Phys. Chem. C* **2010**, *114*, 5822–5826. [CrossRef]
50. Jadhav, S.A.; Somvanshi, S.B.; Khedkar, M.V.; Patade, S.R.; Jadhav, K.M. Magneto structural and photocatalytic behavior of mixed Ni–Zn nano spinel ferrites: Visible light enabled active photodegradation of rhodamine B. *J. Mater. Sci. Mater. Electron.* **2020**, *31*, 11352–11365. [CrossRef]
51. Al-Musawi, T.J.; Mengelizadeh, N.; Al-Rawi, O.; Balarak, D. Capacity and Modeling of Acid Blue 113 Dye Adsorption onto Chitosan Magnetized by Fe_2O_3 Nanoparticles. *J. Polym. Environ.* **2021**, *30*, 344–359. [CrossRef]
52. Enesca, A.; Cazan, C. Polymer Composite-Based Materials with Photocatalytic Applications in Wastewater Organic Pollutant Removal: A Mini Review. *Polymers* **2022**, *14*, 3291. [CrossRef] [PubMed]
53. Matos, R.; Biernacka, I.K.; Rocha, M.; Belo, J.H.; Araújo, J.P.; Estrada, A.C.; Lopes, J.L.; Shah, T.; Korgel, B.A.; Pereira, C.; et al. Design and photo-Fenton performance of Graphene/CuS/Fe_3O_4 tertiary nanocomposites for Rhodamine B degradation. *Catal. Today* **2023**, *418*, 114132. [CrossRef]
54. Tran, V.V.; Nu, T.T.V.; Jung, H.R.; Chang, M. Advanced Photocatalysts Based on Conducting Polymer/Metal Oxide Composites for Environmental Applications. *Polymers* **2021**, *13*, 3031. [CrossRef] [PubMed]
55. Feng, J.; Hou, Y.; Wang, X.; Quan, W.; Zhang, J.; Wang, Y.; Li, L. In-depth study on adsorption and photocatalytic performance of novel reduced graphene oxide-$ZnFe_2O_4$-polyaniline composites. *J. Alloys Compd.* **2016**, *681*, 157–166. [CrossRef]